

## 2D MATERIALS

# Perfect Coulomb drag and exciton transport in an excitonic insulator

Ruishi Qi<sup>1,2,†</sup>, Andrew Y. Joe<sup>1,2,3,\*</sup>, Zuocheng Zhang<sup>1</sup>, Jingxu Xie<sup>1,2</sup>, Qixin Feng<sup>1,2</sup>, Zheyu Lu<sup>1,2</sup>, Ziyu Wang<sup>1,4</sup>, Takashi Taniguchi<sup>5</sup>, Kenji Watanabe<sup>6</sup>, Sefaattin Tongay<sup>7</sup>, Feng Wang<sup>1,2,8\*</sup>

Strongly coupled electron-hole bilayers can host quantum states of interlayer excitons, such as high-temperature exciton condensates at zero magnetic field. This state is predicted to feature perfect Coulomb drag, where a current in one layer is accompanied by an equal but opposite current in the other. We used an optical technique to probe the electrical transport of correlated electron-hole bilayers based on MoSe<sub>2</sub>/hBN/WSe<sub>2</sub> heterostructures. We observed perfect Coulomb drag in the excitonic insulator phase at low temperatures; the counterflow resistance of interlayer excitons remained finite. These results indicate the formation of an exciton gas that does not condense into a superfluid. Our work demonstrates that dynamic optical spectroscopy provides a powerful tool for probing exciton transport behavior in correlated electron-hole fluids.

**A**n electron-hole bilayer—a two-dimensional electron gas (2DEG) and a two-dimensional hole gas (2DHG) coupled together by Coulomb interactions while remaining electrically isolated—provides a highly tunable platform to study strongly correlated electron-hole fluids. In the strong coupling regime where the interlayer distance is small compared with intralayer particle spacing, the electrons and holes in adjacent layers pair into indirect excitons, and the system is expected to host quantum states including correlated excitonic insulators (1, 2), exciton supersolids (3), high-temperature exciton Bose-Einstein condensates (BECs) (2, 4–6), and superfluids (7–10). Such bilayer exciton condensates are characterized by a gapped energy spectrum, spontaneous interlayer phase coherence, and dissipationless exciton transport (4, 11). The interlayer coherence is expected to manifest itself as counterflow superconductivity with perfect Coulomb drag in transport measurements—a current in one layer must be accompanied by an equal but opposite current in the other (12, 13), with a vanishing exciton resistance.

Evidence of exciton condensation and perfect Coulomb drag has been reported in quantum Hall bilayers in semiconductor double quantum wells (12, 14) and graphene systems

(15–17), but the formation of quasi-electrons and quasi-holes in the quantized Landau levels requires a strong external magnetic field, and the excitons only form at very low temperatures (18, 19). Recently, the research focus has shifted toward searching for an exciton condensate in electron-hole bilayers in the absence of a magnetic field (1, 4, 8, 20).

Electron-hole bilayers in semiconducting transition metal dichalcogenide (TMD) heterostructures have attracted special interest because of their strong Coulomb interaction and large exciton binding energy (hundreds of milli-electron volts) (21–24). Consequently, the strong coupling regime becomes accessible (20, 25). When the bandgap energy is electrically tuned below the exciton binding energy, strongly correlated excitonic insulator states have been experimentally achieved (1, 26). Theoretical study of such systems predicts an exciton BEC that persists until a high-temperature Berezinskii-Kosterlitz-Thouless transition (a fraction of the exciton binding energy) (8, 11). Below this temperature, the interlayer excitons are expected to form an exciton superfluid, in which the exciton transports with zero viscosity, similar to the dissipationless transport of Cooper pairs in conventional superconductors. Electrical transport measurements are therefore highly desired to observe these exotic quantum states. However, most semiconducting TMDs have poor electrical contact to common metals due to a large Schottky barrier.

We have developed an optical technique to measure exciton transport behavior without the need to pass any current through contacts. This allows Coulomb drag measurements and quantitative determination of exciton flow resistance. We show that a TMD-based electron-hole bilayer features perfect Coulomb drag—a drive current in one layer induces an equal current in the other layer—at equal electron and hole densities, which becomes nonperfect

but remains strong when additional charges are present. Unexpectedly, our exciton transport measurements show the absence of an exciton superfluid for temperatures down to 2 K, which is in contradiction to many theoretical predictions.

## Optical measurement of resistance and Coulomb drag

Figure 1A schematically shows the device structure and the experimental setup. We choose molybdenum diselenide (MoSe<sub>2</sub>) as the electron layer and tungsten diselenide (WSe<sub>2</sub>) as the hole layer for their type II band alignment. They are separated by a 3-nm thin hexagonal boron nitride (hBN) tunneling barrier to ensure equilibrium electron-hole fluids with negligible interlayer tunneling (fig. S1) (27). The heterostructure is encapsulated by dielectric hBN on both sides and gated by a few-layer graphene top gate (TG) and two bottom gates (BG1 and BG2). This dual-gated electron-hole bilayer device has two regions controlled by separate BGs, each easily tunable with electrical voltages. We began by considering region 1. We kept the electron layer grounded ( $V_e = 0$ ) and applied voltages on the gates and the hole layer. The gate voltage  $V_G \equiv V_{TG} + V_{BG1}$  tunes the Fermi level and thus the net charge density (electron-hole imbalance). The hole-electron voltage difference  $V_h - V_e$  and the vertical electric field  $V_{TG} - V_{BG1}$  both tune the band alignment. Therefore, the effective interlayer bias voltage  $V_B \equiv (V_h - V_e) + \frac{t_m}{t_t + t_m + t_b}(V_{TG} - V_{BG1})$ , where  $t_t$ ,  $t_m$ , and  $t_b$  are top, middle, and bottom hBN thicknesses in region 1, respectively, controls the effective charge gap. Figure 1B is an optical image of such a device (D1), whose detailed structure is given in fig. S2. We define all the electrical voltages using region 1 and scale the dc voltage on BG2 appropriately such that regions 1 and 2 remain in the same gating and electric field conditions, and thus the electron and hole densities remain homogeneous [details in (27)]. Unless otherwise specified, the data discussed hereafter are taken from D1 at a temperature  $T = 2$  K. Similar data have been obtained on device D2, as summarized in fig. S3.

Using reflectance spectroscopy, we were able to determine the doping densities of electrons ( $n_e$ ) and holes ( $n_h$ ) as a function of  $V_G$  and  $V_B$  (26, 27), as shown in Fig. 1, C and D. At low bias voltages, the system has a finite type II bandgap, so only one type of charge can enter the system at a time. When the bias voltage exceeds the gap energy of  $\sim 1.51$  eV, electrons and holes enter the system at the same time, forming correlated electron-hole fluids that consist of interlayer excitons and possibly extra charges (1, 26). In particular, when the bias voltage reduces the single-particle bandgap to be smaller than the exciton binding energy but still non-zero, an excitonic insulator phase emerges that

<sup>1</sup>Department of Physics, University of California, Berkeley, CA, USA. <sup>2</sup>Materials Sciences Division, Lawrence Berkeley National Laboratory, Berkeley, CA, USA. <sup>3</sup>Department of Physics and Astronomy, University of California, Riverside, CA, USA.

<sup>4</sup>School of Physics, Xi'an Jiaotong University, Xi'an, China.

<sup>5</sup>Research Center for Materials Nanoarchitectonics, National Institute for Materials Science, Tsukuba, Japan. <sup>6</sup>Research Center for Electronic and Optical Materials, National Institute for Materials Science, Tsukuba, Japan. <sup>7</sup>School for Engineering of Matter, Transport and Energy, Arizona State University, Tempe, AZ, USA. <sup>8</sup>Kavli Energy NanoScience Institute, University of California, Berkeley, and Lawrence Berkeley National Laboratory, Berkeley, CA, USA.

\*Corresponding author. Email: andrew.joe@ucr.edu (A.Y.J.); fengwang76@berkeley.edu (F.W.)

†These authors contributed equally to this work.

consists of only interlayer excitons, while no extra unpaired charges are allowed to exist owing to the finite single-particle gap (1, 26). The charge compressibility map (26) in Fig. 1E reveals this charge-incompressible triangle region at finite and equal electron and hole densities. In this phase, perfect interlayer correlation is expected at zero temperature. The Coulomb drag is therefore expected to become perfect—any current flow in one layer is necessarily accompanied by an equal but opposite current in the other layer.

In standard electrical transport measurements, multiple contacts are made to each layer to pass currents and measure the resulting voltage drop. However, the contact resistance for TMD layers in the low doping regime is usually orders of magnitude larger than the sheet resistance, and therefore such transport measurements are very challenging. To overcome this problem, we did not drive currents through contacts. Instead, we capacitively drove current between the two heterostructure regions (28) in our device by applying a small voltage modulation  $U = 5$  mV (root-mean-square voltage) at angular frequency  $\omega$  between BG1 and BG2, as illustrated in Fig. 1A. This ac voltage generates an oscillating potential that drives charges and excitons to flow back and forth, leading to

an ac particle density change at  $\omega$ . We then optically detected the density change. The optical absorption of the TMD layers is known to depend sensitively on its local charge density (29, 30). For example, Fig. 1F shows the density dependence of the device reflectivity spectrum near the MoSe<sub>2</sub> A-exciton wavelength. With increasing electron density, the intralayer exciton peak loses its oscillator strength, and an additional absorption peak, commonly known as a trion, appears at lower energy (29–31). We focused a monochromatic laser probe at region 2 (Fig. 1, A and B) and used an avalanche photodiode to read out the reflected light intensity, whose ac component is proportional to the local electron density oscillation  $\Delta n_e$ . Similarly, when the laser wavelength is tuned to the WSe<sub>2</sub> absorption peak, hole density response  $\Delta n_h$  can be measured. The current flow between the two regions,  $I_{e/h}$ , is directly proportional to the optically measured density change,  $I_{e/h} \propto \omega \Delta n_{e/h}$ . The optical response therefore provides a probe for charge and exciton transport behavior for the electron-hole bilayer system.

### Perfect Coulomb drag

Figure 2, A and B, shows the real part of the hole and electron density oscillation averaged

over the low-frequency modulation regime ( $\omega = 0.082$  to 41 kHz). The imaginary part is essentially zero at low frequencies (see fig. S4 for a complete dataset). When the bias voltage is small ( $V_B < 1.51$  V), the system forms a 2DEG or a 2DHG with only one type of charge present. The gate modulation will directly drive the charges in the active layer. The holes (electrons) have a well-defined positive (negative) response, owing to their opposite charge. When a high bias voltage closes the gap and both electrons and holes are present, the experiment turns into a Coulomb drag measurement, where the holes are directly capacitively coupled to the bottom gate modulation and drag the electrons with them. If there were no interlayer coupling and both layers acted as perfect metals, the hole layer would completely screen the gate modulation, and the electron layer would have no response. However, the experimental data show that  $\Delta n_e$  is very strong when both layers are doped, indicating strong interlayer interactions in the electron-hole bilayer. Such strong Coulomb drag, where the drag signal is comparable to the drive signal, is unusual, as most coupled bilayer systems have a drag response that is on the order of a percent or less (32–34). We note that the sign of  $\Delta n_e$  becomes positive in this regime, in contrast to

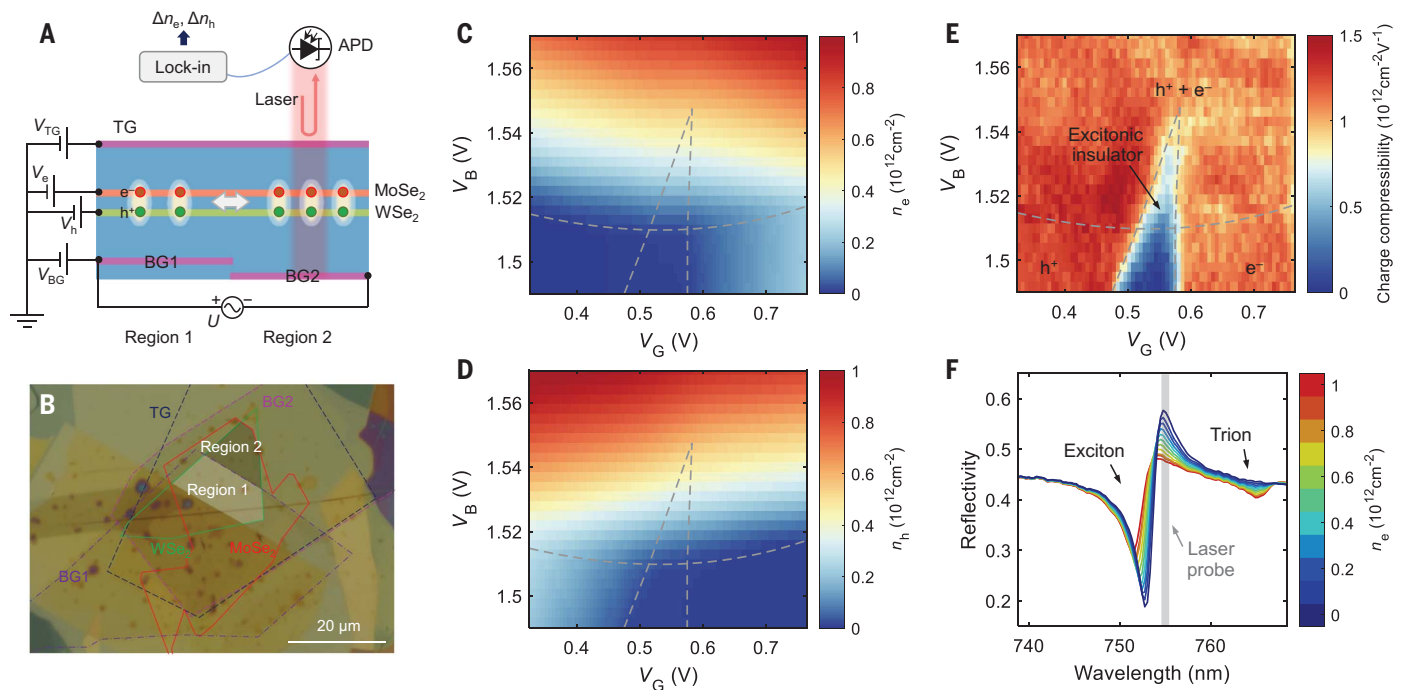


**Fig. 1. Correlated electron-hole bilayer device.** (A) Schematic cross section of device D1, the MoSe<sub>2</sub>/hBN/WSe<sub>2</sub> heterostructure. The magenta, orange, green, and blue layers denote graphite gates, MoSe<sub>2</sub> monolayer, WSe<sub>2</sub> monolayer, and hBN flakes, respectively. The heterostructure has two regions controlled by independent bottom gates (BG1 and BG2). Red and green circles represent electrons and holes, respectively. APD, avalanche photodiode. (B) An optical image of device D1, with flake boundaries outlined. (C and D) Experimentally

determined electron (C) and hole (D) density of the electron-hole bilayer in region 2, measured at temperature  $T = 2$  K (27). (E) Charge compressibility from numerical derivative of electron-hole density imbalance with respect to gate voltage,  $\partial(n_e - n_h)/\partial V_G$ . The dashed lines are a guide to the eye tracing the boundary of different doping regimes. (F) Reflectivity spectrum as a function of electron doping density in the MoSe<sub>2</sub> layer. The gray line marks the wavelength of the laser probe.

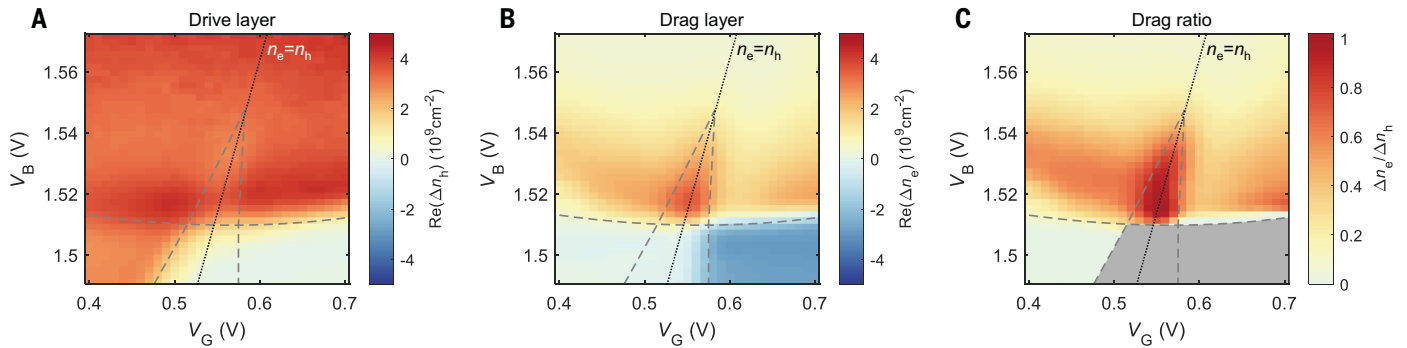


**Fig. 2. Strong Coulomb drag in the electron-hole bilayer.** (A and B) Density change of the drive layer (A) and the drag layer (B) under a low-frequency voltage modulation (averaged for  $\omega = 82$  Hz to 41 kHz), measured at temperature  $T = 2$  K. (C) Drag ratio  $\Delta n_e/\Delta n_h$  as a function of gate and bias voltages. The bottom-right region is grayed out because  $\Delta n_h$  is zero when the hole layer is not doped.

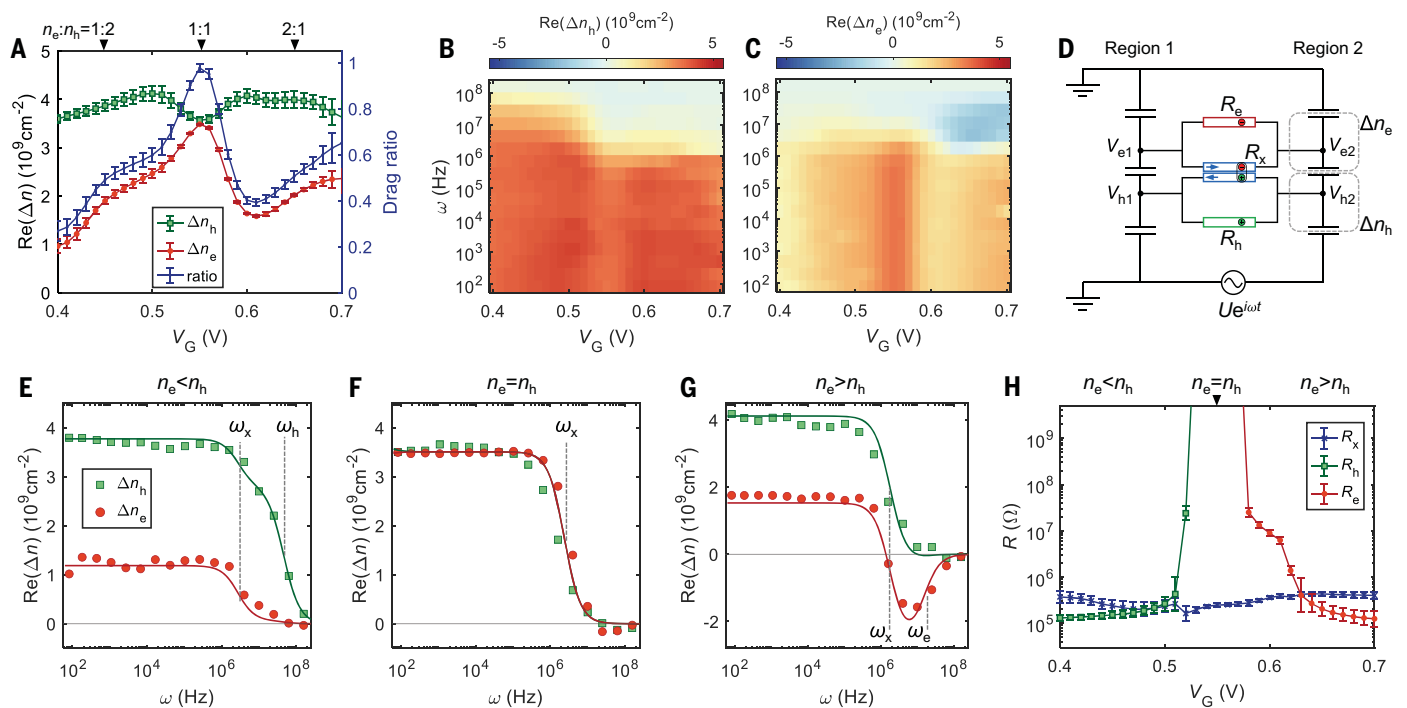


**Fig. 3. Exciton and charge transport.** (A) Drive (green) and drag (red) layer density change as a function of gate voltage at constant  $V_B = 1.52$  V. Right axis (blue): the ratio between  $\Delta n_e$  and  $\Delta n_h$ , revealing perfect Coulomb drag at net charge neutrality. (B and C) Drive and drag layer density change as a function of  $V_G$  under different driving frequencies  $\omega$ . (D) Effective circuit model for transport measurements. (E to G) Frequency sweeps at  $V_G = 0.42, 0.55$ , and  $0.63$  V,

corresponding to three typical doping conditions  $n_e < n_h$ ,  $n_e = n_h$ , and  $n_e > n_h$ , respectively. Squares and circles are experimental data for  $\Delta n_h$  and  $\Delta n_e$ , respectively. Solid lines are fitting results from the effective circuit model (27). (H) Fitted resistance of unpaired electrons ( $R_e$ ), unpaired holes ( $R_h$ ), and interlayer excitons ( $R_x$ ), as a function of  $V_G$ . All data are measured at temperature  $T = 2$  K.

the negative response when there are only electrons in the system. This supports the notion of electrons moving together with holes. For the hole response, the sign remains the same regardless of the electron doping, but the magnitude changes for different doping conditions.

Figure 2C shows the drag ratio  $\Delta n_e/\Delta n_h$ . Noticeably, the drag ratio features a very strong enhancement when the electron and hole densities are equal. In the excitonic insulator phase, we observe substantially increased drag re-

sponse and decreased drive response. The drag ratio approaches unity in this triangle region, which is consistent with an excitonic insulator phase that does not allow unpaired charges at low temperatures.

#### Charge and exciton transport

We next investigated a horizontal linecut at constant bias  $V_B = 1.52$  V (Fig. 3A). Here, the constant  $V_B$  leads to nearly constant  $n_e + n_h \approx 0.3 \times 10^{12} \text{ cm}^{-2}$ , and  $V_G$  tunes the electron-hole imbalance  $n_e - n_h$ . At net charge neutrality  $n_e =$

$n_h$ , the drag signal reaches its peak value, whereas the drive layer has reduced response. Up to our experimental uncertainty, a drag ratio of unity is observed, demonstrating the dominance of exciton transport in the excitonic insulator. When the system is doped with additional electrons or holes, the drag signal decreases rapidly. At zero temperature, the additional electrons or holes are expected to pair with interlayer excitons to create interlayer trions (35, 36), three-particle bound states that resemble hydrogen anions. However, the trion binding

energy is likely on the order of 0.1 meV at 3-nm interlayer distance (35, 37, 38), which is comparable to or smaller than the thermal energy at our base temperature. We do not observe strong peaks in the drag signal at density ratio  $n_e:n_h$  of 1:2 or 2:1, presumably because most trions undergo thermal ionization. The drag behaviors at  $n_e \neq n_h$  stem largely from the transport of excitons and ionized electrons or holes.

The frequency-dependent density change of the hole and the electron layers is displayed in Fig. 3, B and C, respectively. The gate dependence of the signal shows an abrupt change across the net charge neutrality point, indicating strong excitonic effects in the electron-hole bilayer. The responses remain frequency independent below 100 kHz and start to show frequency dependence when further increasing modulation frequency. The frequency dependence can be understood with the effective ac circuit shown in Fig. 3D. Each heterostructure region forms three geometric capacitances (between TG and MoSe<sub>2</sub>, between MoSe<sub>2</sub> and WSe<sub>2</sub>, and between WSe<sub>2</sub> and BG). Ignoring the weak interlayer trion effect, the two heterostructure regions are connected by three effective resistors, corresponding to the transport of unpaired electrons  $R_e$ , unpaired holes  $R_h$ , and interlayer excitons  $R_x$ . Let  $V_{ij}(i \in \{e, h\}, j = 1, 2)$  denote the electrochemical potential of layer  $i$  and region  $j$ . The transport of unpaired electrons and holes can be described by

standard resistors  $R_e$  and  $R_h$ , with current flow  $\frac{V_{e1}-V_{e2}}{R_e}$  and  $\frac{V_{h1}-V_{h2}}{R_h}$ , respectively. The excitons effectively connect the two regions with a special resistor  $R_x$  that carries opposite currents for the two layers,  $\pm \frac{V_{h1}-V_{h2}-V_{e1}+V_{e2}}{R_x}$ , with the WSe<sub>2</sub> layer taking the plus sign and the MoSe<sub>2</sub> layer taking the minus sign. In general, the system forms a resistor-capacitor (RC) circuit with three RC time constants set by  $R_e$ ,  $R_h$ , and  $R_x$ . As the gate modulation frequency increases, each RC system exhibits a characteristic cutoff frequency, beyond which the corresponding carrier motion becomes ineffective. This occurs because the modulation period becomes shorter than the time required for the carriers to complete a full cycle of motion. Therefore, the frequency-dependent response shows a steplike decay behavior. Depending on the order of the three RC constants, the frequency dependence of the charge density response  $\Delta n$  can have multiple steplike features, each step corresponding to the freeze-out of one type of carrier.

The experimentally measured frequency-dependent density response  $\Delta n$  can be fitted to the effective circuit model to extract the values of  $R_e$ ,  $R_h$ , and  $R_x$ . In a strongly coupled bilayer system, the current-voltage relation is determined by a 2-by-2 conductance matrix. The total current, including the contributions from both excitons and unpaired charges, in the MoSe<sub>2</sub> layer and the WSe<sub>2</sub> layer is

$$\begin{bmatrix} I_e \\ I_h \end{bmatrix} = \begin{bmatrix} \frac{1}{R_e} + \frac{1}{R_x} & -\frac{1}{R_x} \\ -\frac{1}{R_x} & \frac{1}{R_h} + \frac{1}{R_x} \end{bmatrix} \begin{bmatrix} V_{e1} - V_{e2} \\ V_{h1} - V_{h2} \end{bmatrix} \quad (1)$$

With this current-voltage relation, the  $(\Delta n_h, \Delta n_e)$  response of the circuit can be solved from basic circuit laws as a function of  $R_e$ ,  $R_h$ , and  $R_x$  and fitted to the experimental data to get  $R_e$ ,  $R_h$ , and  $R_x$  (27). Figure 3, E to G, displays the experimental data (symbols) and corresponding fitting results (solid lines) at three typical doping conditions,  $n_e < n_h$ ,  $n_e = n_h$ , and  $n_e > n_h$ , respectively. We observe qualitatively distinct behavior among the three doping conditions.

When  $n_e = n_h$  (Fig. 3F), the electron and hole responses are identical, with the same amplitude and same cutoff frequency. This demonstrates perfect Coulomb drag in dynamic transport, where the drive current and drag current are identical at all frequencies. The single-step RC decay behavior (determined by  $R_x$ ) is consistent with the excitonic insulator phase that does not have unpaired electrons or holes. When either type of additional charge is present, the responses of the two layers are no longer identical. When  $n_e < n_h$  (Fig. 3E),  $\Delta n_e$  decays at a lower frequency ( $\omega_x$ ) of a few megahertz, but the  $\Delta n_h$  signal survives until a higher cutoff frequency ( $\omega_h$ ) at tens of megahertz. Here  $\omega_x$  is set by exciton

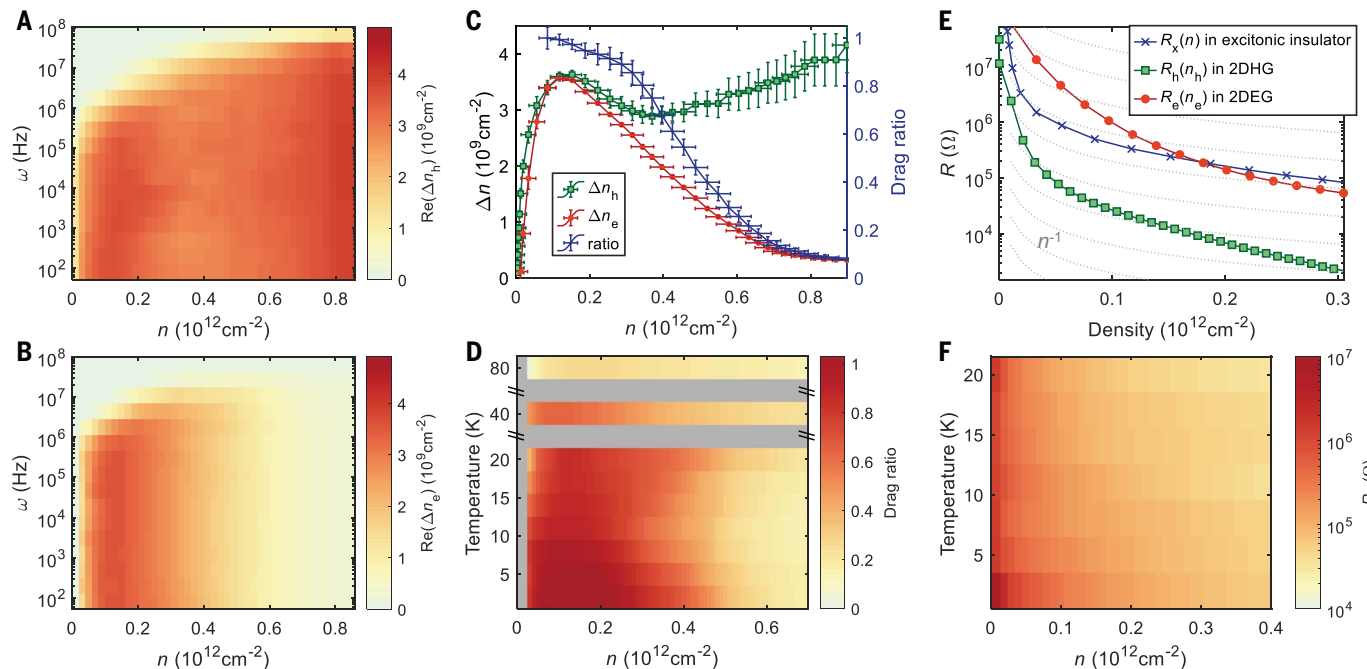


**Fig. 4. Drag behavior and exciton transport at charge neutrality.** (A and B) Density and frequency dependence of the drive and drag layer density change at net charge neutrality ( $n = n_e = n_h$ ) at temperature  $T = 2$  K. (C) Drive (green) and drag (red) layer density change as a function of density  $n$ . Right axis (blue): the ratio between  $\Delta n_e$  and  $\Delta n_h$ . (D) Density and temperature dependence of the drag ratio at net charge neutrality. (E) Fitted exciton

resistance  $R_x$  as a function of  $n$  along the net charge neutrality line shown in blue. Fitted electron (hole) resistance as a function of electron (hole) density in the 2DEG (2DHG) when the opposite charge is not present shown in red (green). Dotted gray lines correspond to constant mobility for reference. (F) Density and temperature dependence of the exciton resistance at net charge neutrality.



motion, whereas  $\omega_h$  is determined by the additional unpaired holes. Between  $\omega_x$  and  $\omega_h$ , the exciton motion becomes ineffective, so  $\Delta n_e$  drops to nearly zero, but the unpaired holes, being more mobile, can still give rise to finite  $\Delta n_h$ . Similarly, for  $n_e > n_h$  (Fig. 3G), there are two steps at different frequencies. The hole layer response  $\Delta n_h$  decays first at a lower frequency  $\omega_x$  beyond which the exciton motion becomes limited. Above  $\omega_x$ , the electron response changes its sign because the electron is pushed away from a negative partial gate rather than being dragged by the positive holes during the exciton transport. This pure electron transport then decays at a higher frequency  $\omega_e$ .

Figure 3H plots the fitted resistances as a function of  $V_G$ . The exciton resistance is on the order of hundreds of kilohms and only has a weak gate dependence across the charge neutrality. The unpaired electron and hole resistance change drastically across net charge neutrality, and they do not become conductive at the same time. When  $n_e < n_h$ ,  $R_e$  is very large and beyond our measurement range, but when  $n_e$  exceeds  $n_h$ , it quickly drops below 1 megohm and decreases with increasing electron density. Similar behavior is observed for the hole resistance. This observation indicates that in the low-density regime, the minority carrier cannot exist in the unpaired form, maximizing the number of interlayer excitons. At net charge neutrality, all the electrons and holes pair into bound states of indirect excitons, and the motion of both free charges becomes frozen, leading to perfect Coulomb drag where the current flow can only come from the exciton motion.

Next, we examined the exciton transport at net charge neutrality. Figure 4, A and B, shows the hole and electron density change as a function of pair density  $n$  and modulation frequency. At low densities, we observe the same response from the two layers, and the drag ratio (Fig. 4C, right axis) is close to unity for  $n \lesssim 0.3 \times 10^{12} \text{ cm}^{-2}$ . With increased density, the drag ratio gradually decreases owing to the reduced single-particle gap and finite thermal energy. It remains considerable even after the Mott density  $n_M \approx 0.8 \times 10^{12} \text{ cm}^{-2}$  (1, 26). Figure 4D shows the temperature dependence of the drag ratio. At low densities, the Coulomb drag ratio remains larger than 85% up to  $\sim 15$  K. It keeps decreasing slowly with increased temperature, indicating the coexistence of excitons, unpaired electrons, and unpaired holes at finite temperatures. After complete thermal melting of interlayer excitons at  $\sim 70$  K (26), the drag signal reduces to only  $\sim 20\%$  at 80 K. The drag signal does not completely disappear after the quantum dissociation at high exciton density or thermal melting at high temperature, suggesting a considerable drag effect in the electron-hole plasma phase caused by strong Coulomb attractions between electrons and holes.

## Discussion and outlook

Fitting the electron and hole responses to the effective exciton circuit model yields the exciton resistance  $R_x$  as a function of pair density  $n$  (Fig. 4E, blue curve). A superfluid transition is not observed. Temperature dependence of the exciton resistance (Fig. 4F) reveals that the exciton resistance decreases with increasing temperature. Contrary to previous theoretical predictions of high-temperature superfluidity in this system (4, 6, 8), we do not observe any signature of an exciton superfluid down to our base temperature  $T = 2$  K. This could possibly be due to disorders in the samples that might destroy the phase coherence between the excitons or an unexpectedly low superfluid transition temperature (11).

Figure 4E compares the resistance of the exciton gas in the excitonic insulator phase (blue), the 2DHG in the WSe<sub>2</sub> layer (green), and the 2DEG in the MoSe<sub>2</sub> layer (red) as a function of carrier density. The resistance of the 2DHG in WSe<sub>2</sub> measured here is consistent with standard four-probe transport results (39), demonstrating the reliability of our optically measured resistance. At similar carrier density, the resistance of excitons in the excitonic insulator phase is always several times higher than that of the 2DHG in the WSe<sub>2</sub> layer and is overall closer to the resistance of the 2DEG in the MoSe<sub>2</sub> layer. Notably, the exciton resistance shows a different density dependence compared with unpaired electrons or holes. The resistance of the 2DHG and the 2DEG both increase substantially faster than  $1/n$  at low density, indicating a reduction of mobility potentially caused by interaction-driven Wigner crystallization or unscreened charge defects (40, 41). In contrast, exciton mobility shows a weaker density dependence. The different scaling behavior suggests a different scattering mechanism for interlayer excitons compared with unpaired charges.

Here, we have demonstrated perfect Coulomb drag in the excitonic insulator phase of the electron-hole bilayer system without any external magnetic field. Our results establish TMD-based electron-hole bilayers as a promising platform for exciton-based electronic devices. Although we did not observe exciton superfluidity in TMD bilayers, our work paves the way for further study of counterflow superconductivity and exciton condensates when the sample quality improves further. The optical technique demonstrated here can provide a way to study transport behaviors in TMD-based systems, especially in the low doping regimes where quantum correlation effects are strong but electrical contacts are difficult to make.

## REFERENCES AND NOTES

1. L. Ma et al., *Nature* **598**, 585–589 (2021).
2. Y. Zeng, A. H. MacDonald, *Phys. Rev. B* **102**, 085154 (2020).
3. S. Conti et al., *Phys. Rev. Lett.* **130**, 057001 (2023).
4. F.-C. Wu, F. Xue, A. H. MacDonald, *Phys. Rev. B* **92**, 165121 (2015).
5. X. Zhu, P. B. Littlewood, M. S. Hybertsen, T. M. Rice, *Phys. Rev. Lett.* **74**, 1633–1636 (1995).

6. Y. E. Lozovik, I. L. Kurbakov, G. E. Astrakharchik, J. Boronat, M. Willander, *Solid State Commun.* **144**, 399–404 (2007).
7. P. Pieri, D. Neilson, G. C. Strinati, *Phys. Rev. B* **75**, 113301 (2007).
8. M. M. Fogler, L. V. Butov, K. S. Novoselov, *Nat. Commun.* **5**, 4555 (2014).
9. J.-J. Su, A. H. MacDonald, *Nat. Phys.* **4**, 799–802 (2008).
10. S. Gupta, A. Kutana, B. I. Yakobson, *Nat. Commun.* **11**, 2989 (2020).
11. B. Debnath, Y. Barlas, D. Wickramaratne, M. R. Neupane, R. K. Lake, *Phys. Rev. B* **96**, 174504 (2017).
12. D. Nandi, A. D. K. Finck, J. P. Eisenstein, L. N. Pfeiffer, K. W. West, *Nature* **488**, 481–484 (2012).
13. B. N. Narozhny, A. Levchenko, *Rev. Mod. Phys.* **88**, 025003 (2016).
14. L. V. Butov, A. Zrenner, G. Abstreiter, G. Böhm, G. Weimann, *Phys. Rev. Lett.* **73**, 304–307 (1994).
15. X. Liu, K. Watanabe, T. Taniguchi, B. I. Halperin, P. Kim, *Nat. Phys.* **13**, 746–750 (2017).
16. J. A. Li, T. Taniguchi, K. Watanabe, J. Hone, C. R. Dean, *Nat. Phys.* **13**, 751–755 (2017).
17. X. Liu et al., *Science* **375**, 205–209 (2022).
18. J. P. Eisenstein, *Annu. Rev. Condens. Matter Phys.* **5**, 159–181 (2014).
19. J. P. Eisenstein, A. H. MacDonald, *Nature* **432**, 691–694 (2004).
20. Z. Wang et al., *Nature* **574**, 76–80 (2019).
21. K. F. Mak, J. Shan, *Nat. Photonics* **10**, 216–226 (2016).
22. G. Wang et al., *Rev. Mod. Phys.* **90**, 021001 (2018).
23. J. Wang et al., *Sci. Adv.* **5**, eaax0145 (2019).
24. J. Wang et al., *Phys. Rev. Lett.* **126**, 106804 (2021).
25. L. A. Jauregui et al., *Science* **366**, 870–875 (2019).
26. R. Qi et al., *Nat. Commun.* **14**, 8264 (2023).
27. See supplementary materials.
28. E. C. Regan et al., *Nature* **579**, 359–363 (2020).
29. K. F. Mak et al., *Nat. Mater.* **12**, 207–211 (2013).
30. J. S. Ross et al., *Nat. Commun.* **4**, 1474 (2013).
31. G. Scuri et al., *Phys. Rev. Lett.* **120**, 037402 (2018).
32. S. Kim et al., *Phys. Rev. B* **83**, 161401 (2011).
33. T. J. Gramila, J. P. Eisenstein, A. H. MacDonald, L. N. Pfeiffer, K. W. West, *Phys. Rev. Lett.* **66**, 1216–1219 (1991).
34. A. F. Croxall et al., *Phys. Rev. Lett.* **101**, 246801 (2008).
35. O. Witham, R. J. Hunt, N. D. Drummond, *Phys. Rev. B* **97**, 075424 (2018).
36. D. D. Dai, L. Fu, *Phys. Rev. Lett.* **132**, 196202 (2024).
37. R. Qi et al., arXiv:2312.03251 [cond-mat.mes-hall] (2023).
38. P. X. Nguyen et al., arXiv:2312.12571 [cond-mat.mes-hall] (2023).
39. J. Pack et al., *Nat. Nanotechnol.* **19**, 948–954 (2024).
40. T. Smoleński et al., *Nature* **595**, 53–57 (2021).
41. Z. Xiang et al., arXiv:2402.05456 [cond-mat.str-el] (2024).
42. R. Qi et al., Perfect Coulomb drag and exciton transport in an excitonic insulator [Dataset], Dryad (2024); <https://doi.org/10.5061/dryad.vhmqg3h>.

## ACKNOWLEDGMENTS

**Funding:** The optical spectroscopy of exciton transport measurements was supported by the AFOSR award FA9550-23-1-0246. The van der Waals heterostructure fabrication was supported by the US Department of Energy, Office of Science, Office of Basic Energy Sciences, Materials Sciences and Engineering Division, under contract DE-AC02-05-CH11231 (van der Waals heterostructures program, KCWF16). S.T. acknowledges support from DOE-SC0020653, NSF CMMI 1933214, NSF mid-scale 1935994, NSF 1904716, and NSF DMR 1552220 and DMR 1955889. K.W. and T.T. acknowledge support from the JSPS KAKENHI (grants 21H05233 and 23H02052) and World Premier International Research Center Initiative (WPI), MEXT, Japan, for the growth of hBN crystals. **Author contributions:** F.W. conceived of the research. R.Q. fabricated the devices with help from A.Y.J., J.X., Q.F., Z.W., and Z.L. R.Q. and A.Y.J. performed optical measurements assisted by Z.Z. and J.X. R.Q., A.Y.J., and F.W. analyzed the data. S.T. grew WSe<sub>2</sub> and MoSe<sub>2</sub> crystals. K.W. and T.T. grew hBN crystals. All authors discussed the results and wrote the manuscript.

**Competing interests:** The authors declare that they have no competing interests. **Data and materials availability:** The data from this study are available at the Dryad repository (42). **License information:** Copyright © 2025 the authors, some rights reserved; exclusive licensee American Association for the Advancement of Science. No claim to original US government works. <https://www.science.org/about/science-licenses-journal-article-reuse>

## SUPPLEMENTARY MATERIALS

[science.org/doi/10.1126/science.adl1839](https://science.org/doi/10.1126/science.adl1839)  
Materials and Methods  
Supplementary Text  
Figs. S1 to S6  
References

Submitted 3 October 2023; accepted 17 December 2024  
10.1126/science.adl1839